



**HAL**  
open science

## Identifying the impact of climate and anthropic pressures on karst aquifers using wavelet analysis

Jean-Baptiste Charlier, Bernard Ladouche, Jean-Christophe Maréchal

### ► To cite this version:

Jean-Baptiste Charlier, Bernard Ladouche, Jean-Christophe Maréchal. Identifying the impact of climate and anthropic pressures on karst aquifers using wavelet analysis. *Journal of Hydrology*, 2015, 523, pp.610-623. 10.1016/j.jhydrol.2015.02.003 . hal-01119955

**HAL Id: hal-01119955**

**<https://brgm.hal.science/hal-01119955>**

Submitted on 24 Feb 2015

**HAL** is a multi-disciplinary open access archive for the deposit and dissemination of scientific research documents, whether they are published or not. The documents may come from teaching and research institutions in France or abroad, or from public or private research centers.

L'archive ouverte pluridisciplinaire **HAL**, est destinée au dépôt et à la diffusion de documents scientifiques de niveau recherche, publiés ou non, émanant des établissements d'enseignement et de recherche français ou étrangers, des laboratoires publics ou privés.

1 **Identifying the impact of climate and anthropic pressures**  
2 **on karst aquifers using wavelet analysis**

3

4

5 **Jean-Baptiste Charlier\***, **Bernard Ladouche** and **Jean-Christophe Maréchal**

6 BRGM, 1039 rue de Pinville, F-34000 Montpellier, France.

7

8 \* Corresponding author: E-mail: [j.charlier@brgm.fr](mailto:j.charlier@brgm.fr); Tel: +33 (0)4 67 15 79 77; Fax: +33 (0)4

9 9 67 64 58 51.

10

11

12

13

14

15 **Abstract**

16 This paper assesses the implications of climate and anthropic pressures on short to long-  
17 term changes in water resources in a Mediterranean karst using wavelet analysis. This  
18 approach was tested on 38-year (1974–2011) hydrogeological time series recorded at the Lez  
19 spring (South France), which is exploited for water supply. Firstly, we investigated inter-  
20 relationships in the frequency domain by cross-correlation across multiresolution levels. Our  
21 results showed that rainfall and spring discharge are highly correlated in the high frequency

22 domain which reflects the hydrogeological response during flood events of typical highly  
23 karstified systems. Pumping and groundwater level are correlated in a lower frequency  
24 domain, illustrating seasonal to multi-year relationships. Secondly, continuous wavelet  
25 transform was applied to characterize the temporal variability of the inter-relationships  
26 involved. On the contrary to examples of “non-managed” karst aquifers in the literature, our  
27 results showed that the 10-year rainfall component was attenuate in the discharge signal. We  
28 assume that the reason is that the storage variations are strongly affected by pumping. This  
29 interesting result shows that possible long-term impacts of rainfall variability due to climate  
30 change may be masked by a high pumping rate. We showed also that despite an increase of  
31 the pumping rate from the 1980s, the stress on the groundwater resource does not increase  
32 from year to year. The present pumping strategy does not affect the drawdown in the long  
33 term, avoiding an over-exploitation of the aquifer. Finally, this study highlights the  
34 effectiveness of wavelet analysis in characterizing the response variability of karst systems  
35 where the hydrogeological regime is modified by pumping.

36

37

## 38 **Keywords**

39 Karst; Wavelet transform; Multiresolution analysis; Hydrogeological processes; Climate and  
40 anthropic pressures; Signal processing

## 41 **1 Introduction**

42 Groundwater is a major global water supply resource and is currently affected by two  
43 main stressors: climate and anthropic pressures. This is essentially true for aquifers pumped  
44 for water supplies in Mediterranean areas due to increased abstraction to meet the needs of the  
45 growing population in regions where the aquifer is irregularly recharged from one year to the  
46 next. Evaluating the impacts of climate and anthropic pressure on water resources in such  
47 regions is a major challenge, as most large aquifers are located in carbonate rocks subject to  
48 karstification. The hydrogeological response of karst systems is highly non-linear due to  
49 spatial and dynamic heterogeneities linked to fact that the void structure leads to the  
50 formation of preferential drainage axes (for reviews see Bakalowicz, 2005; Goldscheider et  
51 al., 2007). Some of karst aquifers are an important water source for major cities, particularly  
52 in Mediterranean regions. In these cases, the aquifer may be referred to as “actively managed”  
53 if the pumping rate is higher than the low water stage discharge rate of the system under  
54 natural conditions in summer. Then, groundwater storage is highly mobilized before the rainy  
55 autumn period that contributes most of the annual recharge each year. In this paper, we  
56 investigate climatic and anthropic impacts on the groundwater resource in a Mediterranean  
57 karst system under active water management. We ask whether pumping modified the  
58 hydrogeological response.

59 Wavelet analysis has become a powerful technique to study geophysical processes or  
60 signals (Kumar and Foufoula-Georgiou, 1997; Torrence and Compo, 1998). Decomposing a  
61 time series into time-scale space, this method localizes power variations within a time series.  
62 It is ideal for analysing non-stationary signals and identifying short- to large-scale periodic  
63 phenomena. In the field of hydrology, Continuous Wavelet Transforms (CWT) have recently

64 been used to study the effect of climatic phenomena on the stream flow regime (Labat et al.,  
65 2005; Massei et al., 2007; Labat, 2010; Fu et al., 2012), or to study runoff processes  
66 (Lafrenière and Sharp, 2003; Schaepli et al., 2007). CWT has been widely used to study the  
67 hydrogeological behaviour of karst systems. Comparing three springs, Labat et al. (2000;  
68 2002) demonstrated the potential of wavelet analysis in identifying karst properties in relation  
69 to the degree of karstification. Structural heterogeneity also determines similar filtering  
70 properties on a small basin scale (Chinarro et al., 2011) and on a large scale (Hao et al.,  
71 2012): i) short time-scale signals are generally less filtered showing the transmissive role of  
72 the conduit network, ii) and high-energy large timescale signals can penetrate through the  
73 aquifer, illustrating the buffered role of the storage zone. In a Mediterranean context, this  
74 allows us to visualize annual and multi-annual scale components in relation to North Atlantic  
75 Oscillation (Andreo et al., 2006). The hydrogeological response has also been studied from a  
76 physico-chemical time series: to investigate transport properties and turbidity dynamics  
77 (Massei et al., 2006), to highlight temperature-runoff relationships during snowmelt  
78 (Mathevet et al., 2004), or to study groundwater variations in relation to the geological  
79 context (Slimani et al., 2009). Surface-groundwater interactions were also studied using CWT  
80 to improve understanding of river flow components in karst environments (Salerno and  
81 Tartari, 2009). But, there is a lack of knowledge regarding the identification of the respective  
82 role of climatic and anthropic pressures on the resource of karst aquifers.

83       Generally, CWT provides a good representation of energy distribution in time-scale  
84 space in all these works, highlighting the non-stationary nature and multi-scale behaviour of  
85 karst systems. However, to overcome limitations arising from intrinsic redundancy of the  
86 CWT representation, Labat et al. (2000; 2001) applied an orthonormal wavelet representation,

87 conserving the signal information, as a complementary approach. This multiresolution  
88 analysis (discrete wavelet transform DWT) can be used to decompose a signal into successive  
89 resolution levels. It allows the energy distribution across levels to be characterized and the  
90 slow and fast components in a spring discharge time series to be distinguished. This  
91 complementary DWT technique allows easier and more efficient interpretation of the energy  
92 distribution across decomposition scales, assisting the study of the time-frequency space of  
93 time series. It can thus greatly improve hydrogeological understanding of karst systems, but is  
94 rarely found in the literature. From these latest studies showing the significant potential of  
95 combined CWT and DWT, we expect that both approaches will be adapted to characterize on  
96 groundwater resources the response to the cumulative effect of climatic and anthropic  
97 pressures.

98       To assess the impacts of climatic and anthropic pressure on groundwater resources in a  
99 karst system under active water management, this study aims to distinguish between the role  
100 of rainfall and pumping on the karst response using wavelet analysis. As a first step, a  
101 multiresolution analysis was performed in order to characterize the energy distribution across  
102 scales. To identify the frequency domain where rainfall and pumping may influence the karst  
103 system, we also present a cross-correlation across multi-resolution levels. As a second step,  
104 continuous wavelet analysis was applied to track changes in phenomena over time, providing  
105 information on the temporal variability of the karst response to climatic and anthropic  
106 stressors. We applied these techniques on rainfall, pumping, discharge and piezometric time  
107 series over a 38-year period (1974–2011) in the Lez aquifer in the South of France.

## 108 **2 Site and measurements**

### 109 **2.1 Study site**

#### 110 **2.1.1 Presentation**

111 The Lez karst is located to the north of Montpellier in the Cévennes area in the South of  
112 France, in the western section of the Mediterranean zone. The Lez karst system is part of the  
113 North Monpelliérains karst hydrogeological unit bounded to the west by the Hérault River  
114 and to the north and east by the Vidourle River (Figure 1). The Lez karst aquifer is located in  
115 Upper Jurassic formations between 650 m and 800 m thick, located on both sides of the  
116 Matelles fault. The aquifer is unconfined to the west of the fault, while the section located to  
117 the east may be partially captive. In the zone lying under a Tertiary overburden, the aquifer is  
118 found in the Upper Jurassic and the Lower Cretaceous. A more detailed description of the  
119 study area can be found in Ladouche et al. (2014).

120 The Lez spring is the main outlet of the karst system (Figure 1). The spring outlet has  
121 been explored by cave-divers. They discovered a huge saturated sub-horizontal karst conduit  
122 developing more than 400 m inland (Figure 2), with a diameter ranging between 5 and 10 m.  
123 The exploration ended at 113 m deep below the spring outlet (-48 m ASL) in a zone where the  
124 conduit become wider. The hydrogeological basin is estimated to cover an area of 380 km<sup>2</sup>  
125 (Thiery et al., 1983). Different recharge zones can be distinguished, depending on the nature  
126 of the geological overburden. Recharge of the aquifer takes place predominantly in Jurassic  
127 limestone, occupying an area of 80 to 100 km<sup>2</sup> (Figure 1). Within the Cretaceous overburden  
128 (120 km<sup>2</sup>), losses occur locally along temporary watercourses and feed the aquifer locally  
129 during flood events. The Tertiary formations occupy an area of about 160 km<sup>2</sup>. In general

130 these are considered as impermeable or almost impermeable and do not contribute to  
131 recharging the Lez karst aquifer.

132 The drinking water supply of the Montpellier agglomeration (with about 340 000  
133 inhabitants) comes from the Lez karst spring since the 19th century (1854). Before 1968, this  
134 resource was used by gravity extraction, varying between  $25 \cdot 10^{-3}$  and  $0.6 \text{ m}^3/\text{s}$  (Paloc, 1979).  
135 From 1968 to today, the Lez karst spring is pumped according an active management strategy,  
136 the pumping flow rate during summer periods is greater than the spring's low-water discharge  
137 so as to mobilize the aquifer's stored reserves (Avias, 1995). From 1968 to 1982, water was  
138 abstracted by pumping in the Lez Spring basin (Figure 2a) at a rate of the order of  $0.8 \text{ m}^3/\text{s}$ .  
139 From 1983 onwards, deep boreholes located in the main karst conduit located upstream from  
140 the spring (Figure 2) have allowed pumping at a rate of up to  $1.7 \text{ m}^3/\text{s}$  (Avias, 1995). The  
141 pumping flow rates during low groundwater levels ( $1.2$  to  $1.7 \text{ m}^3/\text{s}$ ) currently exceed the  
142 pumping flow rates during high groundwater levels ( $0.9 \text{ m}^3/\text{s}$ ). The minimum groundwater  
143 level is fixed at 35 m a.s.l in the main conduit. The maximum drawdown permitted from  
144 pumping is thus 30 m below the overflow threshold of the spring (65 m a.s.l., Figure 2b). The  
145 lowest water level (i.e. 35 m a.s.l.) was reached during the 1995 hydrological cycle. For  
146 environmental reasons, a reserve flow rate of  $0.160 \text{ m}^3/\text{s}$  is restored for the Lez River  
147 downstream of the spring when it is not overflowing.

## 148 **2.1.2 Hydrogeological background**

149 The conceptual scheme of the Lez aquifer, built by Salado and Marjolet (1975) and  
150 completed recently by Bicalho et al. (2012), shows that the water from the Lez spring  
151 comprises a mixture of water from three main units in the aquifer: i) water from the aquifer in  
152 the Upper Jurassic limestone and the Lower Cretaceous; ii) surface water (losses) after



153 interacting with the Cretaceous formations; and iii) water from deep circulation in the  
154 underlying Middle Jurassic, having long residence time.

155 The hydrogeological functioning of the Lez karst system has been characterized using  
156 various rainfall-discharge modelling approaches accounting for pumping (Guilbot, 1975;  
157 Thiery and Bérard, 1984; Fleury et al., 2009). These works showed that pumping during low  
158 water periods draw out reserves coming from less transmissive zones in addition to the well-  
159 drained reserves. An assessment of this pumping influence area around the network of karst  
160 conduits give values of about 60 km<sup>2</sup> (Ladouche et al., 2014), representing only 15% of the  
161 Lez spring's catchment.

162 Recent semi-distributed modelling approaches have given a first assessment of the  
163 contributions of the main karst units. Simulating the groundwater level in the main drain at  
164 the karst outlet using a semi-distributed lumped model, Ladouche et al. (2014) showed that  
165 the eastern part of the Matelles fault is contributing 2-fold higher than the western part. This  
166 result is coherent with previous works of Kong A Siou (2011) applying neuron models in a  
167 semi-distributed approach.

## 168 **2.2 Hydrogeological data**

### 169 **2.2.1 Measured data**

170 Hydrogeological measurements have been carried out since 01 June 1974 to 31  
171 December 2011. Figure 1 shows the locations of the monitoring sites from which data are  
172 used in this study.

173 Daily precipitation intensity was measured in the three weather stations at St-Martin-de-  
174 Londres, Valflaunes and Montpellier-Fréjorgues (Météo France, 2012).

175 Pumping discharge rates ( $Q_p$ ) in the karst conduit near the spring were recorded at daily  
176 intervals from 1974 to 2000, except during the 1991 to 1996 period when measurements were  
177 recorded at weekly intervals. Since 2000,  $Q_p$  has been recorded at hourly intervals.

178 Until 1982, the piezometric level ( $h$ ) was measured in the Lez spring basin at daily  
179 intervals. Since 1983,  $h$  has been measured directly in the main conduit in a borehole located  
180 upstream from the spring (Figure 2). Groundwater levels have been recorded on a daily basis  
181 from 1974 to 2000, except during the 1991-1996 period when measurements were recorded at  
182 weekly intervals. Since 2000,  $h$  has been recorded at hourly intervals. Since  $h$  expresses  
183 groundwater level relative to mean sea level, we also define a drawdown value  $s$  which  
184 expresses the groundwater level measured from the maximum head  $h_{max}$  ( $s(t) = h_{max} - h(t)$ ).  
185 The value  $s$  was used instead of  $h$  in wavelet analysis in order to correlate an increased  
186 pumping rate with increased groundwater fluctuation (as the pumping rate increase is  
187 inversely correlated with the piezometric level).

188 Measured discharge at the Lez spring is denoted residual discharge ( $Q_r$ ), because the  
189 gauging station (Banque Hydro, 2010) is located 300 m downstream the outlet were pumping  
190 are carried out (Figure 2).  $Q_r$  was measured between 1987 and 2007 at daily intervals. Data  
191 were corrected from the restored discharge ( $0.160 \text{ m}^3/\text{s}$ ) to the Lez River when the spring was  
192 dry. Before 1987,  $Q_r$  was estimated from water level measurements in the basin. Minimum  
193  $Q_r$  value is zero.

### 194 **2.2.2 Calculated data**

195 Precipitation data ( $P$ ) used in this study is the rainfall time series calculated by  
196 Ladouche et al. (2014) to optimize the contribution of three rain gauges in their developed  
197 transfer model used to simulate the spring discharge. The method - given by Pinault and

198 Allier (2007) - requires to compute the weighting factor of each rain gauge in order to  
199 maximize the cross-correlation (see Section 3.1 for equations) between  $P$  and residual  
200 discharge ( $Q_r$ ) measured between 1987 and 2007. The linear combination obtained for  $P$  is:

201 (Eq. 1) 
$$P = 0.33P_1 + 0.54P_2 + 0.13P_3$$

202 where  $P_1$  is the precipitation at St-Martin-de-Londres,  $P_2$  is the precipitation at Valflaunes,  
203 and  $P_3$  is the precipitation at Montpellier-Fréjorgues (Figure 1).

204 During high water period - when overflows are observed at the spring (residual  
205 discharge  $Q_r > 0$ ) - pumping is inferior to the natural discharge ( $Q_n$ ).  $Q_r$  is interpreted as the  
206 difference between  $Q_n$  and  $Q_p$ :  $Q_r = Q_n - Q_p$ . According to Ladouche et al. (2014), pumping  
207 mobilizes water stored only in the large conduit (where pumps are localised) during this  
208 period, because no drawdown related to pumping was observed on piezometric  $h(t)$  time  
209 series, as well as in the more distant connected piezometer Claret well (see Fig. 1 for  
210 location). Consequently, during high water period, we assume that the storage flow mobilized  
211 by pumping ( $Q_s$ ) is negligible (almost equal to 0).

212 During low water period - when pumping has dried the spring ( $Q_r = 0$ ) - pumping is  
213 superior to  $Q_n$ , and  $Q_p$  is interpreted as the sum of  $Q_n$  and the  $Q_s$  (Ladouche et al., 2014):  $Q_p$   
214 =  $Q_n + Q_s$ . Pumping thus mobilizes water reserves in the karst system that are inaccessible or  
215 almost inaccessible in natural conditions. This phenomenon is reflected in a decrease of the  
216 piezometric level in the karst conduit (groundwater level < 65 m a.s.l., Figure 2b).

217 The storage flow mobilized by pumping  $Q_s$  is calculated by equation 2 (Ladouche et al.,  
218 2014):

219 (Eq. 2) 
$$\begin{aligned} & \text{if } Q_p \geq Q_n \text{ then } Q_s = Q_p - Q_n \text{ and } Q_r = 0 \\ & \text{if } Q_p < Q_n \text{ then } Q_s \approx 0 \text{ and } Q_r = Q_n - Q_p \end{aligned}$$

220 This last equation requires to assess  $Q_n$  which is unknown during low water level  
221 periods, as the Lez spring has been used since 1854 to supply drinking water (Paloc, 1979).  
222 During high water level periods (Figure 2a),  $Q_n$  is higher than the pumping rate ( $Q_p$ ), and can  
223 be calculated as follows:  $Q_n = Q_r + Q_p$ . During periods of low water levels (Figure 2b),  $Q_n$   
224 cannot be estimated from measurements. Recently, Ladouche et al (2014) have simulated the  
225  $Q_n$  time series using a transfer model combining a fast and a slow impulse response. Impulse  
226 responses were calculated by inverse modelling during high flow periods when  $Q_n = Q_r +$   
227  $Q_p$ . The whole  $Q_n$  time series was then simulated from 1974 to 2011 using the Tempo  
228 software (Pinault, 2001 ; Pinault et al., 2001a, b).

229 All hydrogeological time series for rainfall ( $P$ ), Lez discharge ( $Q_r$  and  $Q_n$ ), pumping  
230 discharge ( $Q_p$ ) and piezometric levels ( $h$ ) for the period from 01 June 1974 to 31 December  
231 2011 were synchronized at a time interval of 1 day.

### 232 **2.2.3 Hydrogeological variables used to assess the karst response to** 233 **stressors**

234 This section presents the hydrogeological variables used as input and output to  
235 characterize the response of the karst system to climatic and anthropic stressors. Table 1  
236 provides an overview of the set of variables, also showing the framework for interpreting their  
237 possible inter-relationships. The purpose of this guide is to help to interpret the results of the  
238 wavelet analysis used in this article.

239 The input variables representing specifically climatic pressure and anthropic pressures  
240 are precipitation  $P$  and pumping  $Q_p$ , respectively. As the  $Q_s$  variable is defined from  $Q_n$  and  
241  $Q_p$ , (Eq. 2), and  $Q_n$  is highly correlated to  $P$ ,  $Q_s$  integrates these both climatic and anthropic  
242 pressures. With regard to the output variables, the residual discharge  $Q_r$  qualifies the karst

243 response to the rainfall during high flows periods. The water level ( $h$ ) and especially the  
244 drawdown ( $s$ ) qualify the karst stored changes due to inputs solicitation (precipitation and  
245 pumping).

246 Two ambiguous input-output relationships for the defined set of variables were  
247 identified. The  $P-h$  relationship is disrupted by the impact of pumping on the water level  $h$   
248 (major drawdown during the summer). Similarly,  $Qp$  cannot be used to study properly the  
249 impact of pumping on  $Qr$ , since the latest is controlled by both  $P$  and  $Qp$  variables.  
250 Consequently, these two relationships were removed from the presented analysis. We will  
251 focus our analysis on the  $P-Qr$  relationship to assess the impact of the climate pressure on the  
252 karst functioning. The  $Qp-s$  relationship is used to assess the anthropic impact on the  
253 reserves. Finally,  $Qs-Qr$  and  $Qs-s$  relationships are used to assess the vulnerability of the  
254 resource to both climatic and anthropic pressures.

### 255 **3 Wavelet analysis**

256 The functions used are briefly presented on the basis of definitions put forward by  
257 several authors for wavelet analysis in geosciences (Kumar and Foufoula-Georgiou, 1997;  
258 Torrence and Compo, 1998; Labat et al., 2000; Bayazit and Aksoy, 2001; Grinsted et al.,  
259 2004; Jevrejeva et al., 2003; Maraun and Kurths, 2004). Wavelet transform can be used to  
260 decompose a time series over a time-scale space, thus providing a visualization of power  
261 distribution along time and frequency. It is suitable for analysis of non-stationary processes  
262 that contain multi-scale features, detection of singularities, or transient phenomena (see the  
263 review of Kumar and Foufoula-Georgiou, 1997). Thus, wavelet analysis gives a time-scale  
264 representation of the processes and of their relationships.

### 265 **3.1 Continuous wavelet transforms**

266 The wavelet transform can be seen as a bandpass filter of uniform shape and varying  
267 location and width (Torrence and Compo, 1998). The continuous wavelet transform (CWT)  
268  $W_x(\tau, a)$  of a time series  $x(t)$  is given as follows:

269 (Eq. 3) 
$$W_x(\tau, a) = \int_{-\infty}^{+\infty} x(t) \Psi_{\tau,a}^*(t) dt$$

270 (Eq. 4) where 
$$\Psi_{\tau,a} = \frac{1}{\sqrt{a}} \Psi\left(\frac{t-\tau}{a}\right)$$

271 represents a group of wavelet functions,  $\Psi_{\tau,a}$ , based on a mother wavelet  $\Psi$  which can be  
272 scaled and translated, modifying the scale parameter  $a$  and the translation parameter  $\tau$   
273 respectively.  $\Psi_{\tau,a}^*$  corresponds to the complex conjugate of  $\Psi_{\tau,a}$ . Wavelet functions have multi-  
274 scale properties, dilating or contracting  $a$  ( $a>1$ ;  $a<1$ ). When  $a$  increases, the wavelet covers a  
275 higher signal window. It allows the large-scale behaviour of  $x$  to be extracted. Conversely,  
276 when  $a$  decreases, the analysed signal window decreases, allowing local variations of  $x$  to be  
277 studied. Wavelet transform is thus characterized on the space scale by a window decreasing in  
278 width when we focus on local scale structures (high frequency), and widening when we focus  
279 on large scale structures (low frequency).

280 As in the Fourier analysis, a wavelet power spectrum (WPS) (also called a scalogram)  
281  $P_x(\tau, a)$  can be defined as the wavelet transform of  $W_x(\tau, a)$ :

282 (Eq. 5) 
$$P_x(\tau, a) = (W_x(\tau, a) W_x^*(\tau, a)) = |W_x(\tau, a)|^2$$

283 The choice of the appropriate analysis wavelet depends on the nature of the signal and  
284 on the type of information to be extracted from the time series (De Moortel et al., 2004). In  
285 this paper, we use the Morlet wavelet, as it is fairly well localized in both time and frequency  
286 space (Torrence and Compo, 1998). Other wavelet basis functions, such as Paul and Mexican

287 hat (DOG), were also tested in order to obtain better time localization, but gave the fairest  
 288 results in both cases. Statistical significance level was estimated against a red noise model  
 289 (Torrence and Compo, 1998, Grinsted et al., 2004). As CWTs are applied to time series of  
 290 finite length, edge effects may appear on the scalogram, leading to the definition of a cone of  
 291 influence (COI) as the region where such effects are relevant (Torrence and compo, 1998).  
 292 The COI is marked as a shadow in the scalogram.

293 The covariance of two time series  $x$  and  $y$  is estimated using a cross wavelet spectrum  
 294 (XWT) (also called a cross scalogram)  $W_{xy}(\tau, a)$ , which is the convolution of the scalogram of  
 295 both signals:

296 (Eq. 6) 
$$W_{xy}(\tau, a) = \left( W_x(\tau, a) W_y^*(\tau, a) \right)$$

297 XWT reveals an area with a high common power value, but Maraun and Kurths (2004)  
 298 reported that it appears unsuitable for significance testing of the interrelation between two  
 299 series. These authors recommend the use of wavelet coherence (WTC) which is a measure of  
 300 the intensity of covariance of the two series in the time-scale space. Beginning with the  
 301 approach of Torrence and Webster (1999), the WTC of two time series  $x$  and  $y$  is defined as:

302 (Eq. 7) 
$$C_{xy}^2(\tau, a) = \frac{|S(a^{-1}W_{xy}(\tau, a))|^2}{S(a^{-1}|W_x(\tau, a)|^2) \cdot S(a^{-1}|W_y(\tau, a)|^2)}$$

303 where  $S$  is a smoothing operator in both time and scale (see Torrence and Webster (1999) and  
 304 Jevrejeva et al. (2003) for detailed mathematical expressions). The 5% significance level of  
 305 WTC against red AR1 noise is estimated using Monte Carlo methods (Grinsted et al., 2004).

306 Neighbouring scales and times contain redundance information and are correlated  
 307 (Maraun and Kurths, 2004), since the wavelet is translated continuously. However, some

308 approaches exist to limit this redundancy, as is the case with Discrete wavelet analysis (Labat  
 309 et al., 2000; Bayazit and Aksoy, 2001) based on a wavelet with an orthogonal form.

### 310 **3.2 Discrete wavelet transform and multiresolution analysis**

311 In order to implement the wavelet transform on sampled signals, the discrete wavelet  
 312 transform (DWT) can be used to discretize the scale and location parameters  $j$  and  $k$ ,  
 313 respectively. The discrete form of the wavelet transform of a time series  $x(t)$  is given  
 314 according to Eq. 8:

315 (Eq. 8) 
$$W_x(\tau_0, a_0) = \sum_{-\infty}^{+\infty} x(t) \Psi_{\tau_0, a_0}^*(t) dt$$

316 (Eq. 9) where 
$$\Psi_{\tau_0, a_0} = \frac{1}{\sqrt{a_0^j}} \Psi\left(\frac{t - k a_0^j \tau_0}{a_0^j}\right)$$

317 with  $a_0^j$  being the scale parameter,  $\tau_0$  the translation parameter,  $k$  and  $j$  integers.  $\Psi_{\tau_0, a_0}^*$   
 318 corresponds to the complex conjugate of  $\Psi_{\tau_0, a_0}$ .

319 Multiresolution analysis (MRA) is able to study of signals represented at different  
 320 resolutions. It can be used to decompose a signal into a progression of successive  
 321 approximations and details in increasing order of resolution. Choosing particular values of  $a_0$   
 322 and  $\tau_0$ , in Eq. 8, namely  $a_0 = 2$ , and  $\tau_0 = 1$ , corresponds to the dyadic case used in MRA. The  
 323 aim is to reduce/increase the resolution by a factor of 2 between two scales. Therefore, the  
 324 approximation of a signal  $x(t)$  at a resolution  $j$ , denoted by  $A_x^j$ , and the detail of the same  
 325 function at a resolution  $j$ , denoted by  $D_x^j$ , are defined by:

326 (Eq. 10) 
$$A_x^j(t) = \sum_{k=-\infty}^{+\infty} C_{j,k} \Psi_{j,k}(t)$$

327 (Eq. 11) 
$$D_x^j(t) = \sum_{k=-\infty}^{+\infty} D_{j,k} \Phi_{j,k}(t)$$



328 where  $\Phi_{j,k}(t)$  is a scaled and translated basis function called the scaling function, which  
329 is determined with  $\Psi_{j,k}(t)$  when a wavelet is selected.  $C_{j,k}$  is the scaling coefficient given the  
330 discrete sampled values of  $x(t)$  at resolution  $j$  and location  $k$ . It is calculated from  $\Phi_{j,k}(t)$  in a  
331 similar way for the wavelet coefficient  $D_{j,k}$  from  $\Psi_{j,k}(t)$  (see Kumar and Foufoula-Georgiou  
332 (1997) for detailed mathematical expressions).

333 The signal  $x(t)$  can be reconstructed from the approximation and detail components as:

334 (Eq. 12) 
$$x(t) = A_x^j(t) + \sum_{j=1}^J D_x^j(t)$$

335 where  $J$  is the highest resolution level considered. Since MRA ensures variance is well  
336 captured in a limited number of resolution levels, analysis of energy distribution in the  
337 sampling time series across scales give a good idea of the energy distribution across  
338 frequencies.

339 The choice of wavelet may influence the decomposition, particularly in low frequencies  
340 (Kumar and Foufoula-Georgiou, 1997). We accordingly tested various wavelet functions  
341 (Haar, Battle, Beylkin, Coiflet, Daubechies, Symmlet, Vaidyanathan) in order to assess the  
342 dispersion of results. Since the results were similar overall in the high frequency domain and  
343 less influenced in the lowest, we opted for the frequently used Daubechies 20 wavelet.

344 In order to quantify the relationship quality between two signals across scales, we used  
345 a multiresolution cross-analysis, combining multiresolution with cross-correlation (Labat et  
346 al., 2002). Cross-correlation can be used to determine the degree of similarity between two  
347 signals or two components (at the same resolution level for instance). The cross-correlation  
348 function (CCF)  $R_{xy}$  of two time series  $x$  and  $y$ , is calculated as follows:

349 (Eq. 13) 
$$R_{xy}(m) = \frac{c_{xy}(m)}{\sigma_x \sigma_y}$$

350 (Eq. 14)                      with                      
$$C_{xy}(m) = \begin{cases} \frac{1}{n} \sum_{t=1}^{n-m} (x_t - \bar{x})(y_{t+m} - \bar{y}) & \text{for } m \geq 0 \\ \frac{1}{n} \sum_{t=1}^{n+m} (y_t - \bar{y})(x_{t+m} - \bar{x}) & \text{for } m < 0 \end{cases}$$

351                      where  $C_{xy}$  is the cross-correlogram,  $m$  is the time lag,  $n$  is the length, and  $\bar{x}$ , and  $\sigma_x$ , and  
 352  $\bar{y}$  and  $\sigma_y$ , are the average and the standard deviation of  $x$  and  $y$ , respectively.

353

354                      More treatments of the wavelet transform (both continuous and discrete) and wavelet-  
 355 based multiresolution (multi-scaling) analysis can be found in Chui (1992), Kumar and  
 356 Foufoula-Georgiou (1997), and Mallat (2009) to which the reader is referred for more detail.  
 357 Continuous wavelet analyses (CWT, XWT, and WTC) were carried out using a free Matlab  
 358 software package (Mathworks, Natick, MA) kindly provided by Grinsted et al. (2004) at  
 359 <http://noc.ac.uk/using-science/crosswavelet-wavelet-coherence>. The package includes code  
 360 originally written by C. Torrence and G. Compo, available at:  
 361 <http://paos.colorado.edu/research/wavelets/>, and by E. Breitenberger of the University of  
 362 Alaska, adapted from the freeware SSA-MTM Toolkit: <http://www.atmos.ucla.edu/tcd/ssa/>.  
 363 Multiresolution analysis was carried out using a free Matlab software package provided by  
 364 the WaveLab Development Team and available at <http://statweb.stanford.edu/~wavelab/>.

## 365 **4 Results**

### 366 **4.1 Variability of hydrogeological time series**

367                      This Section aims to describe the main variations over hydrological cycles from daily to  
 368 annual data, in order to help readers to interpret the results of the wavelet analysis given in the  
 369 next Sections 4.2 and 4.3.

#### 370 4.1.1 Daily variability

371 Figure 3a shows daily hydrogeological time series of the Lez karst system over the last  
372 38 years. Overall, the Mediterranean climate has a high rainfall intensity, for example  
373 attaining 177.5 mm/day in autumn 1976. The mean pumping discharge is around 1 to 1.1  
374 m<sup>3</sup>/s, exceeding the natural baseflow of the Lez spring. To better describe the variability of  
375 other hydrogeological data within a given year, Figure 3b zooms in on the 2002-2003  
376 hydrological year. Heavy rainfall occurs in the end of the summer and in autumn with an  
377 intensity of up to 140 mm/day, generating the highest annual peak flow (15.4 m<sup>3</sup>/s for  $Q_r$ ) at  
378 the Lez spring and a rise in groundwater level ( $h$ ) from 65 to 69 m a.s.l.. In the winter and  
379 spring seasons, lower rainfall intensities generate lowest hydrodynamic response of the karst  
380 system as shown by small flood peaks inferior to 5 m<sup>3</sup>/s and low groundwater variations.  
381 During this period of high groundwater level,  $Q_p$  is near to 1.0 m<sup>3</sup>/s and consistently below  
382  $Q_n$ : the spring is discharging ( $Q_r > 0$ ). At the beginning of the dry season in summer,  $Q_p$   
383 increases to 1.4 m<sup>3</sup>/s and exceeds  $Q_n$ . The spring consequently dries up ( $Q_r$  is zero), and  $h$   
384 starts to decrease (water is pumped directly from the conduit). During the low groundwater  
385 period in summer, the drawdown reaches 25 m (i.e. the piezometric level drops to 40 m a.s.l.).  
386 The saturated zone is highly mobilized by pumping and the reserve storage flow ( $Q_s$ )  
387 increases to high values (around 1.0 m<sup>3</sup>/s). The first abundant autumn rainfall in September  
388 2003 led to rapid groundwater recovery to the initial level of 65 m a.s.l. as observed on the  
389 groundwater level time series ( $h$ ). This phenomenon occurred in less than one day. The spring  
390 then starts to discharge again ( $Q_r > 0$ ) and another similar hydrological cycle begins.

### 391 **4.1.2 Annual variability**

392 To identify humid and dry periods and changes in the pumping discharge on an annual  
393 time scale, Figure 4 shows the annual hydrogeological time series expressed as deviation from  
394 the mean. The highest peaks for precipitation  $P$  occur in 1976-78, 1987-88, 1995-97, 2000-01,  
395 2002-04 and 2008-09. Although annual discharge peaks ( $Q_r$ ) are clearly related to these  
396 humid years, there is no evidence of any relationship with groundwater level ( $h$ ). Regarding  
397 annual pumping ( $Q_p$ ) and karst storage flow mobilized by pumping ( $Q_s$ ), we observed two  
398 periods. From 1974 to 1984 both time series are consistently below the mean (except in 1979-  
399 80 for pumping), unlike the period from 1984 to the present, during which the time series are  
400 higher for most of the time. These periods correspond respectively to a high and a low annual  
401 mean groundwater level, meaning that the groundwater level is primarily linked to pumping,  
402 leading to a rise in  $Q_s$  as pumping rates increase. These results highlight the changes in water  
403 resource management from 1983, when water abstraction from deep boreholes began. This  
404 allows a higher pumping rate, less constrained in terms of drawdown. Before 1983, the  
405 position of the pump in the basin of the spring did not allow the water level to drop to more  
406 than 7 m, as opposed to 30 m today.

## 407 **4.2 Multiresolution analysis**

### 408 **4.2.1 Energy distribution across scales**

409 The main aim of this section is to visualize the distribution of energy across scales (or  
410 resolution levels) of the hydrogeological time series. Multiresolution was performed on daily  
411 data and the results for the first 10 multiresolution levels are shown in Figure 5. Overall,  
412 energy is distributed variably across levels in the hydrogeological time series. Regarding

413 input signals, precipitation  $P$  showed high energy mainly for levels 1 to 4 in the high  
414 frequency domain (corresponding to 1 to 8 days). This means that rainfall events on several  
415 days explain most of the variance in the overall  $P$  signal. The pumping discharge rate  $Qp$   
416 showed high energy at all levels. Daily to weekly  $Qp$  variations are clearly highlighted as  
417 noise in the first levels. For levels 6 to 10, we observed a gradual decrease in energy during  
418 the 1980s. This was clearly visible on raw data (see Figure 3a). As with the pumping signal,  
419 the karst storage flow ( $Qs$ ) showed high energy across levels. On the other hand, it shows a  
420 gradual energy increase in the 1980s. Regarding the output data for the karst system, the both  
421 residual discharge ( $Qr$ ) and groundwater level ( $h$ ) showed high energy distribution across  
422 scales, but different fluctuations over time. For  $Qr$ , energy distribution appears to be related to  
423 flood events for high frequencies (levels 1 to 4, corresponding to 1 to 8 days), and to seasonal  
424 and annual variations for lowest frequencies (levels 8, corresponding to 128 days). Energy  
425 variations for the groundwater level are in the same range regardless of the resolution level,  
426 meaning that scale has no apparent effect on groundwater variance. For all levels,  $h$  energy  
427 fluctuations over time in the 1980s are consistent with the previously observed gradual  
428 increase and decrease of  $Qs$  and  $Qp$  respectively.

429        In order to quantify the energy by multiresolution levels, the standard deviation (s.d.)  
430 was calculated by levels for each standardized time series (Figure 6). Overall, as previously  
431 described,  $P$  energy distribution across levels is totally different from other hydrogeological  
432 data. Figure 6 shows that s.d. of  $P$  decreases from 0.53 to about 0 for low to high  
433 multiresolution levels, meaning that the higher the frequency domain, the higher the energy.  
434 For other time series, we observe a similar main s.d. peak at level 8 (128 days), meaning that  
435 the highest energy is observed for medium levels, corresponding to intra-annual (seasonal)

436 periods. A second, lower s.d. peak is observed at levels 10 (512) and 12 (5.6 years) showing  
437 that high energy is also observed for annual and multi-year periodicities. Nevertheless, the  
438 s.d. of these time series is not negligible in the first levels, meaning that unlike precipitation,  
439 energy is still important across scales.

#### 440 **4.2.2 Multiresolution cross-correlation**

441 To identify the frequency domain where input signals may influence karst system  
442 behaviour, in this section we present a cross-correlation function (CCF) across multiresolution  
443 levels (Figure 7). As shown in Table 1, the input signals used are  $P$ ,  $Qp$ , and  $Qs$  and the  
444 output signals used are  $Qr$ , and  $s$  (instead of  $h$ ). For each plot, two types of CCF were carried  
445 out. In a first case, as proposed by *Labat et al. (2002)*, a CCF was carried out between two  
446 signals at the same multiresolution level  $j$  (black circles). In a second case, we chose to carry  
447 out a CCF between an overall input signal (i.e. a non-decomposed time series) and an isolated  
448 output signal at a given multiresolution level  $j$  (green stars). The maximum cross-correlation  
449 values  $R_{max}$  are shown in Figure 7 as a function of the multiresolution levels of the output  
450 signal expressed in days (at level  $j$ , the resolution corresponds to  $2^{j-1}$  days).

451 In the first case (CCF between two signals at the same multiresolution level), the higher  
452 the multiresolution level, the higher the value of  $R_{max}$  up to 1. In contrast, we observed a  $R_{max}$   
453 peak in the second case (CCF using an overall input signal). This difference shows that the  
454 output signal at a given multiresolution level is strongly influenced by the energy at lower  
455 resolution levels of the input signal. We can thus hypothesize that in the first case the CCF  
456 was controlled mainly by the resolution level of the decomposed times series. The  $R_{max}$  values  
457 of 1 (indicating that the output signal is exactly the same as the input signal) for the highest  
458 multiresolution levels are compatible with this hypothesis. Consequently, only the CCFs

459 between an overall input signal and an isolated output signal at a given multiresolution level  
460 (green stars) were considered for the analysis of multiresolution cross-correlation.

461       Regarding CCF between precipitation values as input and residual discharge values as  
462 output ( $P-Q_r$  plots in Figure 7a), we observe a very similar evolution of  $R_{max}$  across scales.  
463 The highest correlation (around 0.30) occurs for levels 2 and 3, corresponding to 2 and 4-day  
464 resolution periods. This means that time series mainly co-vary in the high frequency domain  
465 on the flood event-time scale. A sill for levels 7 and 8 (64 and 128 days) is observed, leading  
466 the curve to decrease irregularly. This means that highest flood events imprint the discharge at  
467 the seasonal scale. For the highest multiresolution levels, both the rainfall and discharge time  
468 series become uncorrelated.

469       Regarding a CCF between pumping as input and drawdown as outputs ( $Q_p-s$  plots in  
470 Figure 7b), we observe a bimodal distribution of  $R_{max}$  across levels at level 8 (128 days) and  
471 level 13 (11.2 years) with  $R_{max}$  of 0.47 and 0.40, respectively. These results show that time  
472 series co-vary mainly for medium (intra-annual) and high (multi-year) levels, and that data are  
473 uncorrelated in the high frequency domain.

474       Regarding a CCF between storage flows as input and residual discharge and drawdown  
475 as outputs ( $Q_s-Q_r$  and  $Q_s-s$  plots in Figure 7c and 7d, respectively), we observe a similar  
476 bimodal distribution of  $R_{max}$  across scales, compared to the CCF using  $Q_p$  as input. At level 8,  
477 however, the highest correlations using  $Q_s$  as input (0.39 and 0.61 for  $Q_s-Q_r$  and  $Q_s-s$   
478 respectively) showed that  $Q_s$  is a better signal than  $Q_p$  for characterizing the karst response to  
479 anthropic pressure within a given year. This is especially true for  $s$  as an output signal,  
480 because a strong correlation is also observed for the whole spectrum of energy as evidenced

481 by the  $R_{max}$  (0.84) of the CCF using an overall signal for input and output (dotted blue line in  
482 Figure 7d).

### 483 **4.3 Continuous wavelet analysis**

#### 484 **4.3.1 Wavelet power spectrum**

485 Multiresolution cross-correlations provide information on frequency domains which are  
486 or are not correlated between two signals, but give no information on the temporal variability  
487 of their inter-relationships. The aim of this section is to investigate the short- to long-term  
488 influence of climatic and anthropic pressures on the karst response using Morlet continuous  
489 wavelet analysis (CWT). Because multiresolution analysis showed that pumping rate seems to  
490 not influence the hydrogeological response in very high frequencies (several days), CWT was  
491 carried out in the monthly to multi-annual frequency domain, in which anthropic impact may  
492 be investigated. Figure 8 presents scalograms for all hydrogeological variables to assess the  
493 spectral power variance of each hydrogeological signal at each level and at each time lag. On  
494 scalograms, the x- and y-axes represent the time-scale space, with frequencies expressed as  
495 periods in days (high frequencies or low periods at the top of the plot). The z-axis represents  
496 the value of the wavelet coefficient with low to high powers in blue to red colors.

497 Regarding the CWT for rainfall ( $P$  in Figure 8a), we identify structures in the high  
498 frequency domain (less than 128 days) which are not particularly less marked in the case of  
499 spring discharge ( $Qr$  in Figure 8d). This low signal attenuation in the 32 to 128-day band in  
500  $Qr$  highlights a high transmissive function of the infiltration zone of the karst system.  
501 Generally, smallest semi-annual structures (128 to 256 days) appear concomitantly with the  
502 main annual ones during wet hydrological cycles in both  $P$  and  $Qr$  signals (i.e. in 1976-78,



503 1987-88, 1996-98, 2000-01, 2002-04 and 2008-09, see Figure 4). This shows the imprint of  
504 rainfall fluctuations on the karst system in autumn and in a lower manner in spring season. A  
505 scale-dependent structure for a 100 to 500-day period is observed in 1995 for  $P$ , highlighting  
506 the multi-scale distribution of energy among the highest rainfall events. A 10 to 8-year  
507 component is observed from 1991 to 2003 for  $P$ , reflecting a clear variation in large-scale  
508 rainfall distribution. This component is visible in the scalograms of  $Qr$ , but power is not  
509 above the 5% significance level except in the cone of influence (COI). Globally, on the  
510 contrary to high and medium frequencies, these results highlight an attenuation of the lowest  
511 frequencies in rainfall by the karst system. This is coherent with the multiresolution cross-  
512 correlation analysis presented above, showing a poor correlation between rainfall and  
513 discharge in the lowest frequencies.

514       Regarding CWTs for pumping, karst storage flow and groundwater level ( $Qp$ ,  $Qs$ , and  $h$   
515 in Figure 8b, 8c, and 8e, respectively), we identified a high variability of periodic structures  
516 over time before and after 1985. In the three scalograms, components are visible in the high  
517 frequency domain (below 128 days), for a seasonal period (128-256 days) and for an annual  
518 period. However, these structures, visible for  $Qp$  from 1974 to 1985, disappear from 1985  
519 onwards, except for some small-scale and erratic annual structures. At the same time, all these  
520 structures appear for  $Qs$  and  $h$  in 1985 after a period without any visible component. This  
521 result is consistent with the multiresolution analysis showing a gradual decrease in  $Qp$  energy  
522 on all scales before 1985, and a concomitant gradual increase in  $Qs$  and  $h$  energies after this  
523 date. Again, the change in energy distribution observed since 1985 is related to the change in  
524 the water resource operating strategy since the creation of deep boreholes in 1983. On the

525 contrary to rainfall, no significant long-scale structures are visible in these three scalograms,  
526 despite high power in low frequencies of  $Qp$  and  $s$ .

### 527 **4.3.2 Cross wavelet and coherence analysis**

528 Inter-relationships between signals are investigated using cross wavelet transform  
529 (XWT) and wavelet coherence (WTC). Figure 9 presents cross-scalograms between rainfall,  
530 pumping and karst storage flow (as input signals) and spring discharge and groundwater level  
531 (as output signals) to help characterize the response of the system.

#### 532 **4.3.2.1 Response to climatic variations**

533 Responses to climatic variations were investigated for XWT and WTC between  
534 precipitation as input and residual discharges as outputs ( $P-Qr$  plots in Figure 9a and 9b).  
535 Except for the driest years (notably 1990-1993) coinciding with low wavelet power,  
536 significant coherence between  $P$  and  $Qr$  appears throughout the time-scale space, suggesting  
537 strong relationships between both time series at all scales. XWT highlighted an irregular  
538 annual component during wet years when seasonal structures are also visible. Common  
539 features from the CWT stand out as being significant on the 8 to 10-year band from 1978 to  
540 2005, showing a strong link between  $P$  and  $Qr$ .

#### 541 **4.3.2.2 Response to anthropic variations**

542 Responses to anthropic pressure were investigated for XWT and WTC between  
543 pumping as input and drawdown as outputs ( $Qp-s$  plots in Figure 9c and 9d). The  $Qp-s$   
544 scalogram showed an irregular annual component during mean and dry years when the  
545 surplus is not recharged, emphasizing the impact of pumping on the karst aquifer. Seasonal  
546 and high frequencies are also visible irrespective of the hydrological cycle (dry or wet)

547 showing that  $Qp$ - $s$  relationships within a given year are not dependent on the annual recharge  
548 rate. No long-term influence is visible on the  $Qp$ - $s$  scalogram.

#### 549 **4.3.2.3 Response to the cumulative effect of climatic and anthropic variations**

550 Responses to the cumulative effect of climatic and anthropic variations were  
551 investigated for XWT and WTC between karst storage flow as input and residual discharges  
552 and drawdown as outputs ( $Qs$ - $Qr$  plots in Figure 9e and 9f, and  $Qs$ - $s$  plots in Figure 9g and  
553 9h). For both the  $Qs$ - $Qr$  and  $Qs$ - $s$  cross-scalograms, two main components are clearly visible  
554 at 6 months and 1 year from 1985, showing a high level of co-variance between abstraction  
555 from groundwater storage and residual discharge and drawdown from the implantation year of  
556 the pumps directly in the karstic drain. For XWT  $Qs$ - $Qr$ , the 6-month component appears  
557 more irregular since it is only visible when the karst system dries rapidly during the spring  
558 when the winter and spring recharge is insufficient to maintain a baseflow discharge above  
559 the pumping rate ( $Qs > 0$  when  $Qn < Qp$ ). For XWT  $Qs$ - $s$ , we observed significant coherence  
560 throughout the time-scale space, showing strong relationships between both time series at all  
561 scales. Here, it is interesting to note that no significant common features in the wavelet power  
562 is visible in lowest frequencies, despite high coherence.

## 563 **5 Discussion**

564 The aim of this study was to identify using wavelet analysis the respective impacts of  
565 climatic and anthropic pressures on the water resource of a karst system under active water  
566 management. The first challenge was to identify the contributions of both stressors (namely  
567 rainfall and pumping rate, respectively) which concomitantly influence the hydrogeological

568 response. The second challenge was to track the evolution of phenomena over time and thus  
569 to identify the parameters leading to changes in the hydrogeological response of the system.

## 570 **5.1 Frequency domains in which stressors influence the karst** 571 **response**

572 Multiresolution analysis (MRA) showed varying energy distribution across levels,  
573 meaning that the karst response was highly variable from high to low frequencies. Using  
574 multiresolution cross correlation, we determined the frequency domain where output signals  
575 (discharge and groundwater level) were most closely correlated to input signals (rainfall and  
576 pumping). Our results showed that rainfall and spring discharge are highly correlated in the  
577 high frequency domain which reflects the hydrogeological response during flood events of  
578 typical highly karstified systems. Pumping and storage flow are correlated to discharge and  
579 drawdown in the medium and low frequency domains, illustrating seasonal to multi-year  
580 relationships.

## 581 **5.2 Climatic impact**

582 Continuous wavelet transform (CWT) were used as a complementary approach of MRA  
583 to track tendencies and potential evolutions of the hydrogeological response. For rainfall and  
584 discharge CWTs, we showed that (i) high rainfall intensities are restored as in the discharge  
585 signal during flood events, (ii) an annual component is only visible during wet years in both  
586 signals (i.e. when extreme rain events occur), and (iii) the 10-year rainfall component was  
587 attenuate in the discharge signal. Despite this attenuation of the lowest frequencies observed  
588 in rainfall CWT, cross-wavelet transform (XWT) and coherence (WTC) were useful to  
589 provide evidence of long-term climate impacts on spring discharge. This 10-year component

590 should be related to rainfall oscillation in the 5 to 10-year band outlined by Pinault (2012) in  
591 the western Mediterranean region. The attenuation of the large-scale rainfall component is  
592 clearly different from examples of “non-managed” hydrosystems in the literature (Labat et al.,  
593 2000; Chinarro et al., 2011; Hao et al., 2012), which showed that in general karst systems  
594 filter less high frequencies ( $< 2$  months) as in our study case, but imprint highly the lowest  
595 frequencies due probably to inertial processes generated by the storage volume. Likely  
596 explanations of the opposite process at large-scale observed in the Lez karst system is the  
597 pumping strategy within a given year that regulates the storage variations (increasing or  
598 decreasing the pumping rate according to the available water resource). This interesting result  
599 shows that possible long-term impacts of rainfall variability due to climate change on the  
600 karst system may be masked by the high pumping rate. However, we showed that XWT and  
601 WTC may be a useful approach in order to detect it. The question thus arises of whether  
602 pumping can modify the hydrogeological regime of the karst system.

### 603 **5.3 Anthropic impact**

604 Comparing multiresolution results and those of scalograms, a gradual increase in power  
605 distribution was observed for the groundwater level in the 1980s and was concomitant with  
606 the gradual increase and decrease in power observed for pumping  $Q_p$  and storage flow  $Q_s$   
607 respectively. This evolution is generated by the change in pumping strategy since the creation  
608 of deep boreholes in 1983, when pumps were placed directly in the saturated zone of the  
609 conduit. We assessed the frequency space of this evolution in terms of cross-scalograms and  
610 coherence.

611 The impact of pumping on the hydrogeological response was characterized using  $Q_p$ - $s$   
612 XWTs. An irregular annual component was observed during mean and dry years on the

613 scalogram when there is no extra-recharge. Moreover, no large-scale component was  
614 highlighted, meaning that any trend exists on the hydrogeological response to pumping. In  
615 fact, regulations impose a maximum drawdown in the Lez aquifer (30 m below the spring),  
616 limiting the impact of pumping on storage, even after the increase of pumping rate in 1983.

617 Cross wavelet analysis and coherence showed that  $Q_s$  is a better signal than  $Q_p$  to  
618 explain the piezometric levels, with  $Q_s$  reflecting both anthropic and climatic pressures as it  
619 displays storage mobilization (i.e. pumping during periods of low groundwater levels). For  
620 both  $Q_s-Q_r$  and  $Q_s-s$  cross-scalograms, two main components are clearly visible at 6 months  
621 and 1 year from 1983. Regarding the  $Q_s-s$  cross-scalogram, the annual and 6-monthly  
622 components appear continuous from 1983 to date, excluding irregularities in the 6-monthly  
623 component during wet years. Multi-scale structures are also visible from 2 months to 1 year,  
624 illustrating the scale-dependence of both series. This illustrates the anthropic and climatic  
625 cumulative effects on the storage level, with continuous annual stress from the starting date of  
626 active management. The absence of a large scale component between  $Q_s$  and  $s$  (and between  
627  $Q_s$  and  $Q_r$ ) can be explained by two phenomena: i) the high recharge rate during autumn in  
628 Mediterranean areas, refilling the saturated zone each year, and ii) the pumping restriction  
629 imposed by regulations stipulating the maximum drawdown. In this setting, the stress on the  
630 groundwater resource does not increase from year to year and the present pumping strategy  
631 does not affect the drawdown in the long term, avoiding an over-exploitation of the aquifer.

## 632 **5.4 Implications on the understanding of the karst hydrogeological** 633 **response**

634 Multiresolution cross-analysis combined with cross wavelet analysis helps to improve  
635 our understanding of hydrogeological processes. Relationships between pumping  $Q_p$  and  
636 groundwater level  $s$ , and between storage flow mobilized by pumping  $Q_s$  and  $s$ , give  
637 informations on the storage evolution over time. Regarding multiresolution levels, we  
638 observed that  $Q_p$  and  $Q_s$  have a mainly mid- to long-term influence on the piezometric level  
639 in the conduit. In view of the continuous pumping strategy, we may assume that water stored  
640 in the fissured rock matrix is highly mobilized by pumping in the conduit during low water  
641 level periods. This is consistent with the results of Ladouche et al. (2014) which showed that  
642 the pumping induces mobilization of water in less transmissive units. In fact, conduit/matrix  
643 relationships generated by pumping have soon been observed during a 1-month pumping test  
644 in the Cent-Fonts karst system (Southern France) by Maréchal et al. (2008). The authors  
645 showed that both the fissured matrix (several kilometers away from the pumping well) and the  
646 conduit network were affected by the test. Indeed, pumping at the Lez aquifer outlet may  
647 influence the upstream part of the karst system over a long distance of about 20 km  
648 (Ladouche et al., 2014). The Matelles fault (location shown in Figure 1) is a major drainage  
649 axis and the direction of groundwater flow in the Lez aquifer has been ascertained by means  
650 of artificial tracer experiments (Marjolet and Salado 1975; Bérard 1983) and by interpretation  
651 of monitored water levels measured along this fault (especially at the Claret well - Figure 1)  
652 (Karam 1989; Conroux, 2007).

## 653 **6 Conclusion**

654       The aim of this study was to assess the respective impact of climatic and anthropic  
655 pressures on groundwater resources in a Mediterranean karst system under active water  
656 management. The main interest in our study was a combination of discrete (multiresolution)  
657 and continuous wavelet on 38-year hydrogeological time series recorded at the managed Lez  
658 karst aquifer (South France). Our main results showed that water management modifies the  
659 hydrogeological response at short and large-time scales. We assume that the reason why  
660 large-scale rainfall component do not appear in the spring discharge is that groundwater  
661 storage is highly affected by pumping. This result shows that possible long-term impacts of  
662 rainfall variability due to climate change may be masked by a high pumping rate. Despite an  
663 increase of the pumping rate from the 1980s, the stress on the groundwater resource does not  
664 increase from year to year. The current regulation of the hydrogeological conditions by  
665 controlling the drawdown – and thus the pumping rate - may be the reason why no long-term  
666 anthropic influence was identified. This indicates that the aquifer is currently not over-  
667 exploited. Thus, in case necessary, we expect that an increase of the pumping rate is again  
668 possible. This study highlights the effectiveness of wavelet analysis in characterizing the  
669 response variability of karst systems where the hydrogeological regime is modified by  
670 pumping. In order to establish water management scenarios under climatic changes, our  
671 approach may be useful to help decompose time series, extracting frequencies in which  
672 climatic and anthropic components are mainly localised, before their use in modelling  
673 approaches.

674



## 675 **Acknowledgements**

676 This work was conducted under the “Impact Karst” development project funded by  
677 BRGM. The authors wish to thank the *Montpellier Agglomération*, the Rhone-Mediterranean  
678 and Corsica Water Agency, the *Conseil Général de l’Hérault*, and the *Région Languedoc-*  
679 *Roussillon* for funding this work as part of the Lez-GMU project, and to thank Veolia for  
680 sharing time series data.

## 681 **References**

682 Andreo, B., P. Jiménez, J.J. Dura, F. Carrasco, I. Vadillo, and A. Mangin (2006),  
683 Climatic and hydrological variations during the last 117–166 years in the south of the Iberian  
684 Peninsula, from spectral and correlation analyses and continuous wavelet analyses. *J. Hydrol.*  
685 324: 24–39.

686 Avias, J. (1995), Active management of Lez karstic spring, Herault, France, 1957–1994.  
687 *Hydrogeologie*, Editions du BRGM, pp. 113–128.

688 Bakalowicz, M. (2005), Karst groundwater: a challenge for new resources. *Hydrogeol.*  
689 *J.*, 13, 148–160.

690 Banque Hydro (2010), <http://www.hydro.eaufrance.fr>; station No. Y3204020.

691 Bayazit, M, and H. Aksoy (2001). Using wavelets for data generation, *Journal of*  
692 *Applied Statistics*, 28(2), 157-166.

693 Bérard, P. (1983), Alimentation en eau de la ville de Montpellier. Captage de la source  
694 du Lez. Etude des relations entre la source et son réservoir aquifère. Rapport n°2 Définition  
695 des unités hydrogéologiques, BRGM Montpellier.

696 Bicalho, C.C., C. Batiot-Guilhe, J.L. Seidel, S. Van Exter, H. Jourde (2012),  
697 Geochemical evidence of water source characterization and hydrodynamic responses in a  
698 karst aquifer. *J. Hydrol.*, 450–451: 206–218.

699 Chinarro, D., J. L. Villarroya, and J. A. Cuchi (2011), Wavelet analysis of Fuenmayor  
700 karst spring, San Julian de Banzo, Huesca, Spain. *Environ. Earth Sci.*, 65:2231–2243.

701 Chui, C.K. (1992), *An Introduction on Wavelets*, Academic Press, San Diego, 264 p.

702 Conroux, Y. (2007), *Caractérisation du fonctionnement hydrodynamique de l’aquifère*  
703 *karstique du Lez à l’état naturel. Mémoire Master 2, Univ. Avignon 2*, 151 p.

704 De Moortel, I., S.A. Munday, and A. W. Hood (2004), Wavelet analysis: The effect of  
705 varying basic wavelet parameters. *Solar Physic.*, 222:203-228.

706 Fleury, P., B. Ladouche, Y. Conroux, H. Jourde, and N. Dörfliger (2009), Modelling the  
707 hydrologic functions of a karst aquifer under active water management – The Lez spring. *J.*  
708 *Hydrol.*, 365(3-4):235-243.

709 Fu, C., A. L. James, and M. P. Wachowiak (2012), Analyzing the combined influence  
710 of solar activity and El Niño on streamflow across southern Canada, *Water Resour. Res.*, 48,  
711 W05507.

712 Goldscheider, N., D. Drew, and S. Worthington (2007), Introduction. In: Goldscheider,  
713 N., Drew, D. (Eds.), *Methods in Karst Hydrogeology*, Taylor & Francis, London. *Int. Contrib.*  
714 *Hydrogeol.* 26, 1–8.

715 Grinsted, A., J. Moore, and S. Jevrejeva (2004), Application of the cross wavelet  
716 transform and wavelet coherence to geophysical time series. *Nonlinear Process. Geophys.*,  
717 11(5-6): 561–566.

718 Guilbot, A. (1975), Modélisation des écoulements d'un aquifère karstique (Liaison  
719 pluie-débit). Application aux bassins de Saugras et du Lez. PhD thesis, Université des  
720 Sciences et Techniques du Languedoc (Montpellier).

721 Hao, Y., G. Liu, H. Li, Z. Li, J. Zhao, and T.-C. J. Yeh (2012), Investigation of karstic  
722 hydrological processes of Niangziguan Springs (North China) using wavelet analysis. *Hydrol.*  
723 *Process.*, 26, 3062–3069.

724 Jevrejeva, S., J. C. Moore, and A. Grinsted (2003), Influence of the Arctic Oscillation  
725 and El Niño-Southern Oscillation (ENSO) on ice conditions in the Baltic Sea: The wavelet  
726 approach, *J. Geophys. Res.*, 108(D21), 4677, doi:10.1029/2003JD003417.

727 Karam, Y. (1989), Essai de modélisation des écoulements dans un aquifère karstique.  
728 Exemple de la source du Lez (Hérault, France). PhD thesis, Université Montpellier II  
729 Sciences et Techniques du Languedoc, 210 p.

730 Kong A Siou, L. (2011), Modélisation des crues de bassins karstiques par réseaux de  
731 neurones. Cas du bassin du Lez (France). PhD thesis, Univ. Montpellier 2, 230p.

732 Kumar P, Foufoula-Georgiou E. 1997. Wavelet analysis for geophysical applications.  
733 *Reviews of Geophysics* 35(4): 385–412.

734 Labat, D., R. Ababou, and A. Mangin (2000), Rainfall–runoff relations for karstic  
735 springs. Part II: continuous wavelet and discrete orthogonal multiresolution analyses, *J.*  
736 *Hydrol.*, 238: 149–178.

737 Labat, D., R. Ababou, and A. Mangin (2001), Introduction of wavelet analyses to  
738 rainfall–runoffs relationship for karstic basins: the case of Licq–Atherey karstic system  
739 (France), *Ground Water*. 39(4): 605–615.

740 Labat, D., R. Ababou, and A. Mangin (2002), Analyse multirésolution croisée de pluies  
741 et débits de sources karstiques. *C. R. Geoscience* 334: 551–556.

742 Labat, D., J. Ronchailb, and J. L. Guyot (2005), Recent advances in wavelet analyses:  
743 Part 2 – Amazon, Parana, Orinoco and Congo discharges time scale variability. *J. Hydrol.*,  
744 314: 289–311.

745 Labat, D. (2010), Cross wavelet analyses of annual continental freshwater discharge and  
746 selected climate indices. *J. Hydrol.*, 385: 269–278.

747 Ladouche, B, J.-C. Maréchal, and N. Dörfliger (2014). Semi-distributed lumped model  
748 of a karst system under active management, *J. Hydrol.*, 509, 215-230.

749 Lafrenière, M., and M. Sharp. (2003), Wavelet analysis of inter-annual variability in the  
750 runoff regimes of glacial and nival stream catchments, Bow Lake, Alberta. *Hydrol. Process.*  
751 17, 1093–1118.

752 Mallat, S. (2009), *A wavelet tour of signal processing. The sparse Way.* 3d Edition.  
753 Academic Press, 805p. ISBN 13:978-0-12-374670-1

754

755 Maraun, D., and J. Kurths (2004), Cross wavelet analysis: significance testing and  
756 pitfalls. *Nonlinear Process. Geophys.* 11, 505–514.

757 Marechal, J.C., Ladouche, B., Doerfliger, N., Lachassagne, P., 2008. Interpretation of  
758 pumping tests in a mixed flow karst system. *Water Resour. Res.* 44, W05401,  
759 doi:10.1029/2007WR006288

760 Marjolet, G. and J. Salado (1975), Contribution à l'étude de l'aquifère karstique de la  
761 source du Lez (Hérault). III. Etude des écoulements d'eau dans les calcaires fissurés et

762 karstifiés du site du futur captage de la source du Lez. Université Montpellier II. Mémoires du  
763 C.E.R.G.A, Tome IX-Fac. III. 139p.

764 Massei, N., J.P. Dupont, B.J. Mahler, B. Laignel, M. Fournier, D. Valdes, and S. Ogier  
765 (2006), Investigating transport properties and turbidity dynamics of a karst aquifer using  
766 correlation, spectral, and wavelet analyses. *J. Hydrol.*, 329: 244– 257.

767 Massei, N., A. Durand, J. Deloffre, J. P. Dupont, D. Valdes, and B. Laignel (2007),  
768 Investigating possible links between the North Atlantic Oscillation and rainfall variability in  
769 northwestern France over the past 35 years, *J. Geophys. Res.*, 112, D09121,  
770 doi:10.1029/2005JD007000.

771 Mathevet, T., M. Lepiller, and A. Mangin (2004), Application of time series analyses to  
772 the hydrological functioning of an Alpine karst system: the case of Bange-L'Eau-Morte.  
773 *Hydrology and Earth System Sciences*. 8(6): 1051-1064.

774 Météo France (2012), Rainfall data, 1974–2011. METEO France, Toulouse, France

775 Paloc, H. (1979), Alimentation en eau de la Ville de Montpellier. Captage de la source  
776 du Lez, commune de St-Clément (Hérault). Etude documentaire préalable à l'établissement  
777 des périmètres de protection. Note de synthèse. Rapport BRGM 79 SGN 319 LRO, 47p.

778 Pinault, J.L., 2001. Manuel utilisateur de TEMPO, logiciel de traitement et de  
779 modélisation des séries temporelles en hydrogéologie et en hydrogéochimie. BRGM, Report  
780 RP-51459-FR, 221 p.

781 Pinault, J.-L., H. Pauwels, and C. Cann (2001a), Inverse modeling of the hydrological  
782 and the hydrochemical behavior of hydrosystems; application to nitrate transport and  
783 denitrification. *Water Resour. Res.* 37(8):2179-90.

784 Pinault, J.-L., V. Plagnes, L. Aquilina, and M. Bakalowicz (2001b), Inverse modeling of  
785 the hydrological and the hydrochemical behavior of hydrosystems; characterization of karst  
786 system functioning. *Water Resour. Res.* 37(8):2191-204.

787 Pinault, J.-L., and D. Allier (2007), Regionalization of rainfall for broad-scale  
788 modeling: An inverse approach, *Water Resour. Res.*, 43, W09422.

789 Pinault, J.-L. (2012), Global warming and rainfall oscillation in the 5–10 yr band in  
790 Western Europe and Eastern North America. *Climatic Change*: 114:621–650. DOI  
791 10.1007/s10584-012-0432-6.

792 Salado, J. and G. Marjolet (1975), Contribution à l'étude de l'aquifère karstique de la  
793 source du Lez (Hérault). II. Etude du chimisme des eaux de la source du Lez et de son bassin.  
794 Université Montpellier 2. Mémoires du C.E.R.G.A, Tome IX-Fac. II. 101p.

795 Salerno, F., and G. Tartari (2009), A coupled approach of surface hydrological  
796 modelling and Wavelet Analysis for understanding the baseflow components of river  
797 discharge in karst environments. *J. Hydrol.*, 376: 295–306.

798 Schaefli, B., D. Maraun, and M. Holschneider (2007), What drives high flow events in  
799 the Swiss Alps? Recent developments in wavelet spectral analysis and their application to  
800 hydrology. *Advances in Water Resources* 30: 2511–2525.

801 Slimani S, Massei N, Mesquita J, Valdés D, Fournier M, Laignel B, Dupont JP. 2009  
802 Combined climatic and geological forcings on the spatio-temporal variability of piezometric  
803 levels in the chalk aquifer of Upper Normandy (France) at pluridecennial scale. *Hydrogeology*  
804 *Journal* 17: 1823–1832

805 Thiery, D., P. Bérard, and A. Camus (1983), Captage de la source du Lez. Etude de  
806 relation entre la source et son réservoir aquifère – rapport n°1 : recueil des données et  
807 établissement d’un modèle de cohérence. Rapport BRGM 83SGN 167 LRO

808 Thiery, D., and P. Bérard (1984), Alimentation en eau de la Ville de Montpellier -  
809 Captage de la source du Lez. Etude des relations entre la source et son réservoir aquifère –  
810 rapport n°3 : modèle d’étude détaillé. Rapport BRGM 84-AGI-171-LRO/EAU

811 Torrence, C., and G.P. Compo (1998), A practical guide to wavelet analysis. Bull. Am.  
812 Met. Soc. 79, 61–78.

813 Torrence, C., and P.J. Webster (1999), The annual cycle of persistence in the El Niño/  
814 Southern Oscillation. Quart. J. R. Met. Soc. 124: 1985–2004.

815

816 Table 1: Guide to hydrological variables providing keys to interpret the response of the  
 817 hydrological system to stressors; relationships underlined in grey are used in the present  
 818 study.

819

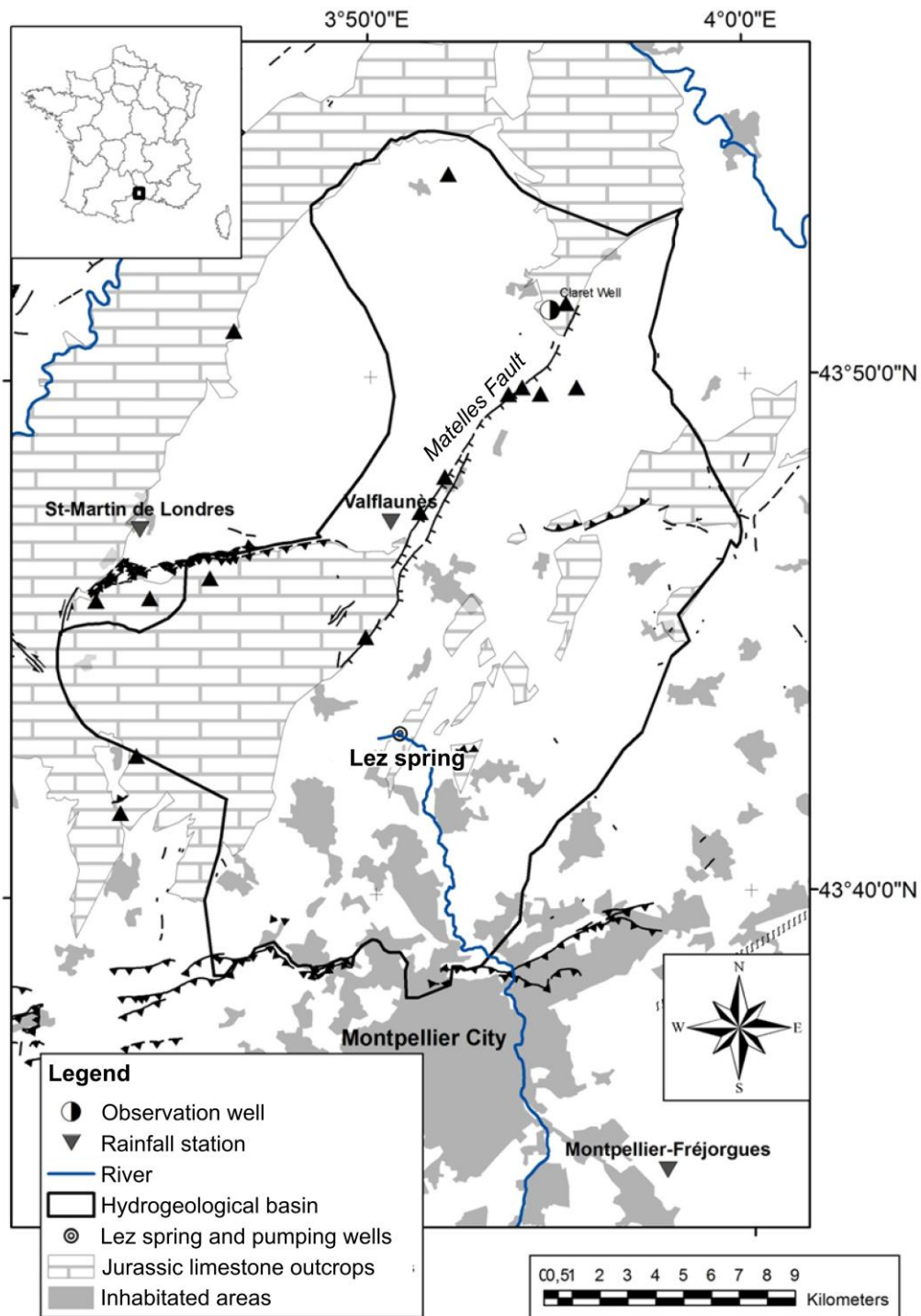
Stressors		Karst response		
Input variable used to characterize stressors		Output variable used to characterize the karst response		
		<i>Q<sub>r</sub></i>	<i>h</i> or <i>s</i>	
		Residual discharge	Groundwater level or drawdown	
Climatic pressure	<b>P</b> Precipitation	<i>Input-Output relationships</i>	<b><i>P-Q<sub>r</sub></i></b>	<b><i>P-h</i> or <i>P-s</i></b>
		<i>Highlight:</i>	Hydrogeological response	<i>Relationship disrupted by pumping</i>
Anthropic pressure	<b>Q<sub>p</sub></b> Pumping discharge	<i>Input-Output relationships</i>	<b><i>Q<sub>p</sub>-Q<sub>r</sub></i></b>	<b><i>Q<sub>p</sub>-s</i></b>
		<i>Highlight:</i>	<i>Relationship disrupted by precipitation</i>	Storage mobilization
Climatic and anthropic pressures	<b>Q<sub>s</sub></b> Karst storage flow mobilized by pumping	<i>Input-Output relationships</i>	<b><i>Q<sub>s</sub>-Q<sub>r</sub></i></b>	<b><i>Q<sub>s</sub>-s</i></b>
		<i>Highlight:</i>	Groundwater stress due to active water management during low groundwater level periods	Level of stress on the groundwater resource

820

821



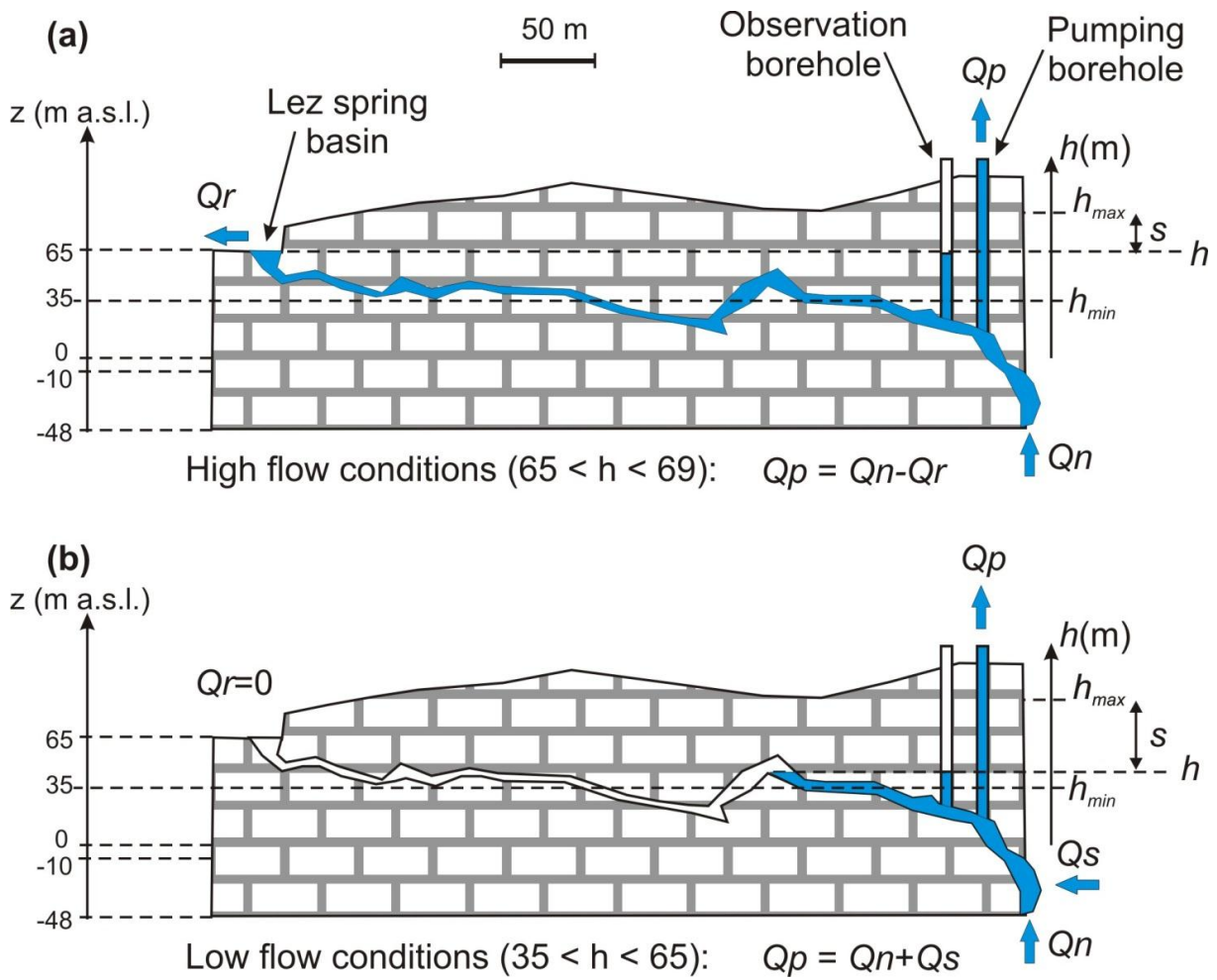
822 Figure 1: Hydrogeological map of the Lez karst system.



823

824

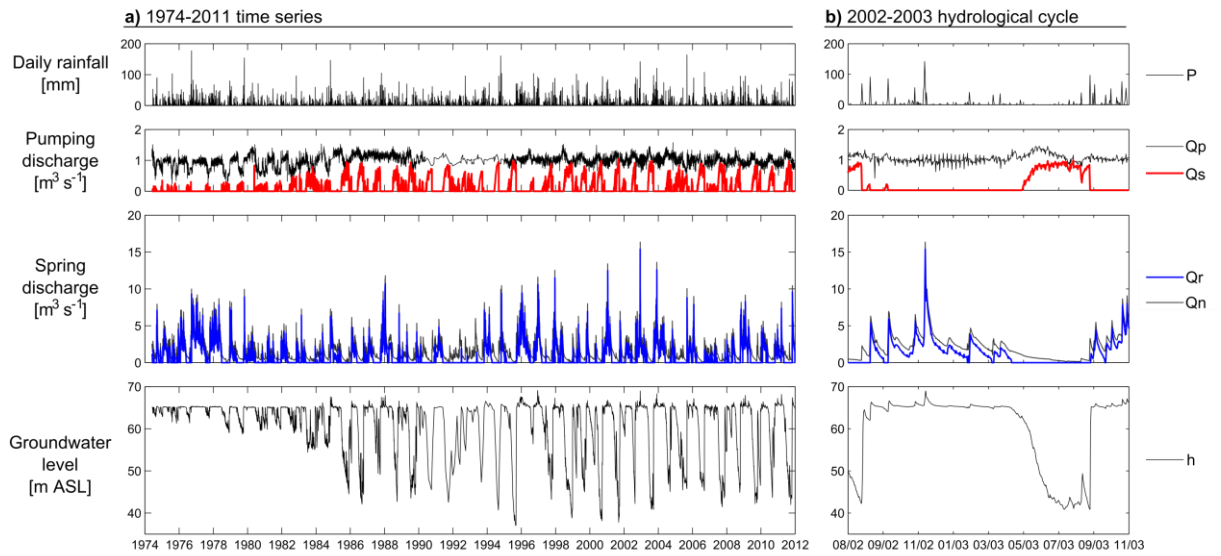
825 Figure 2: Cross section of the karst network at the outlet of the Lez aquifer, showing the  
 826 location of the spring and of the pumping station; Piezometric levels are also plotted  
 827 according to high (2a) and low (2b) flow conditions.



828

829

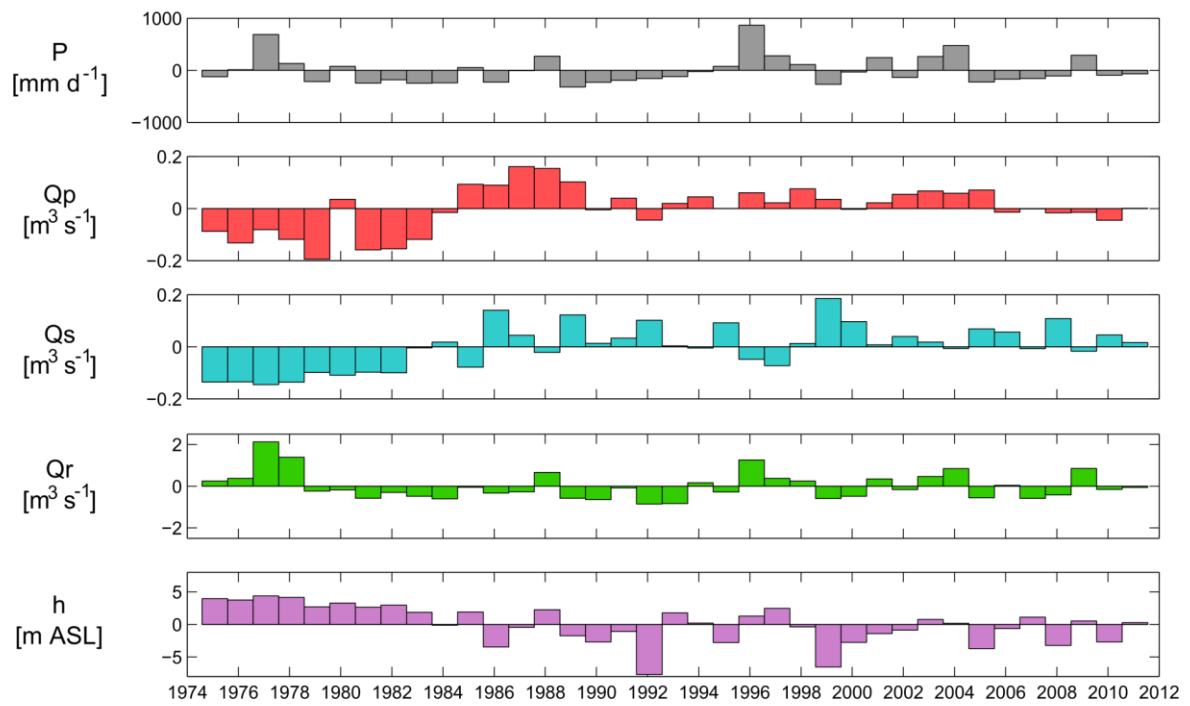
830 Figure 3: Hydrogeological daily time series of the Lez karst system from 01 June 1974 to 31  
 831 December 2011 (a), and a zoom on the 2002-2003 hydrological cycle (b); from top to bottom:  
 832 precipitation ( $P$ ), measured pumping discharge ( $Q_p$ ) and calculated storage discharge  
 833 mobilized by pumping ( $Q_s$ ), measured Lez residual discharge ( $Q_r$ ) and simulated natural  
 834 discharge ( $Q_n$ ), and the measured groundwater level in the conduit ( $h$ ).



835

836

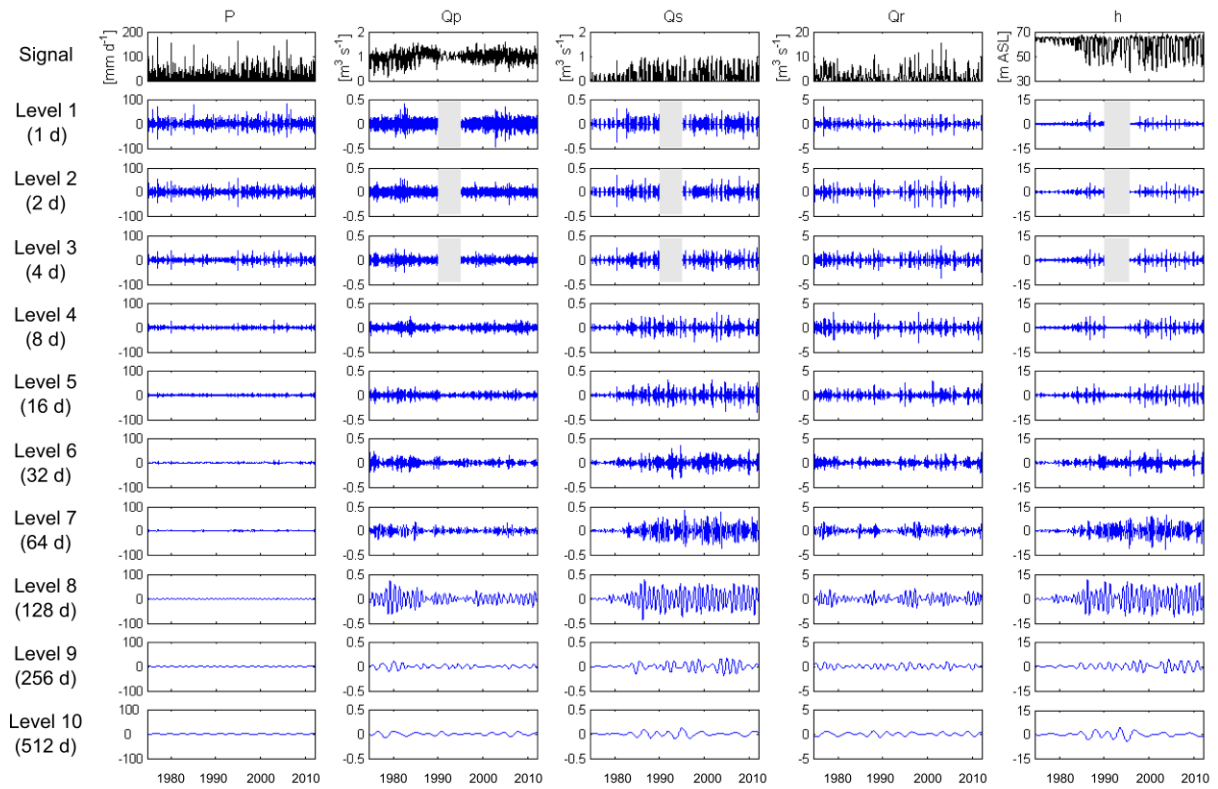
837 Figure 4: Annual evolution of hydrogeological time series expressed as deviation from the  
838 mean; the annual hydrological cycle was delimited from August to July.



839

840

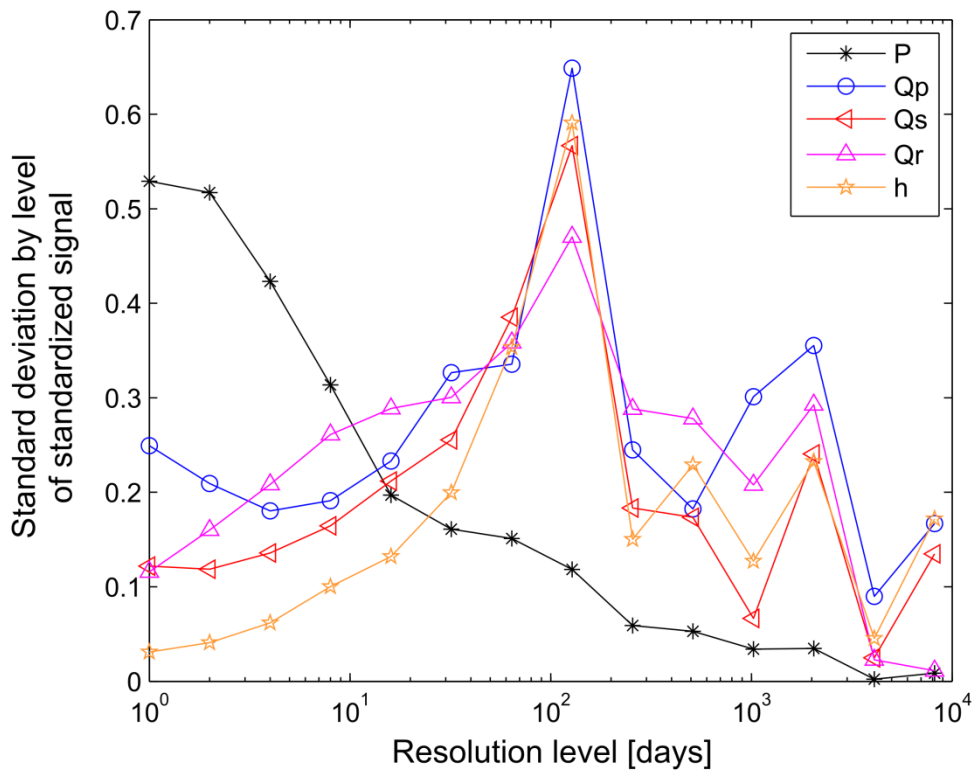
841 Figure 5: Multiresolution analysis of daily hydrogeological time series using Daubechies 20  
 842 wavelets; different components of the decomposition correspond from top to bottom to short-  
 843 scale to long-time scale processes, with level  $j$  corresponding to time scales at  $2^{j-1}$ ; grey  
 844 rectangles indicate a lack of data for the first levels 1 to 3 (1 to 4-day resolution) during a  
 845 period of weekly raw data.



846

847

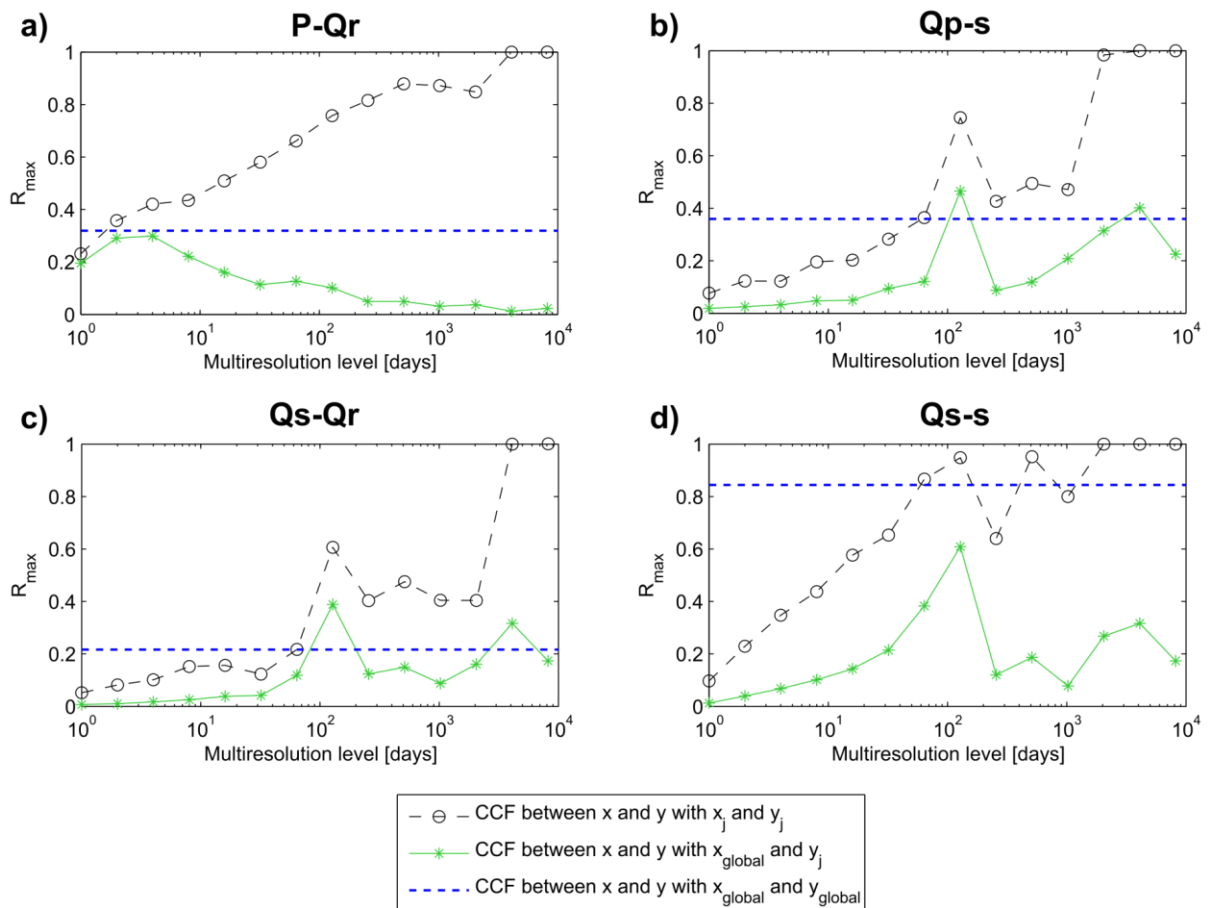
848 Figure 6: Standard deviation by multiresolution levels (from level 1 to level 14) of the  
849 standardized hydrogeological signals.



850

851

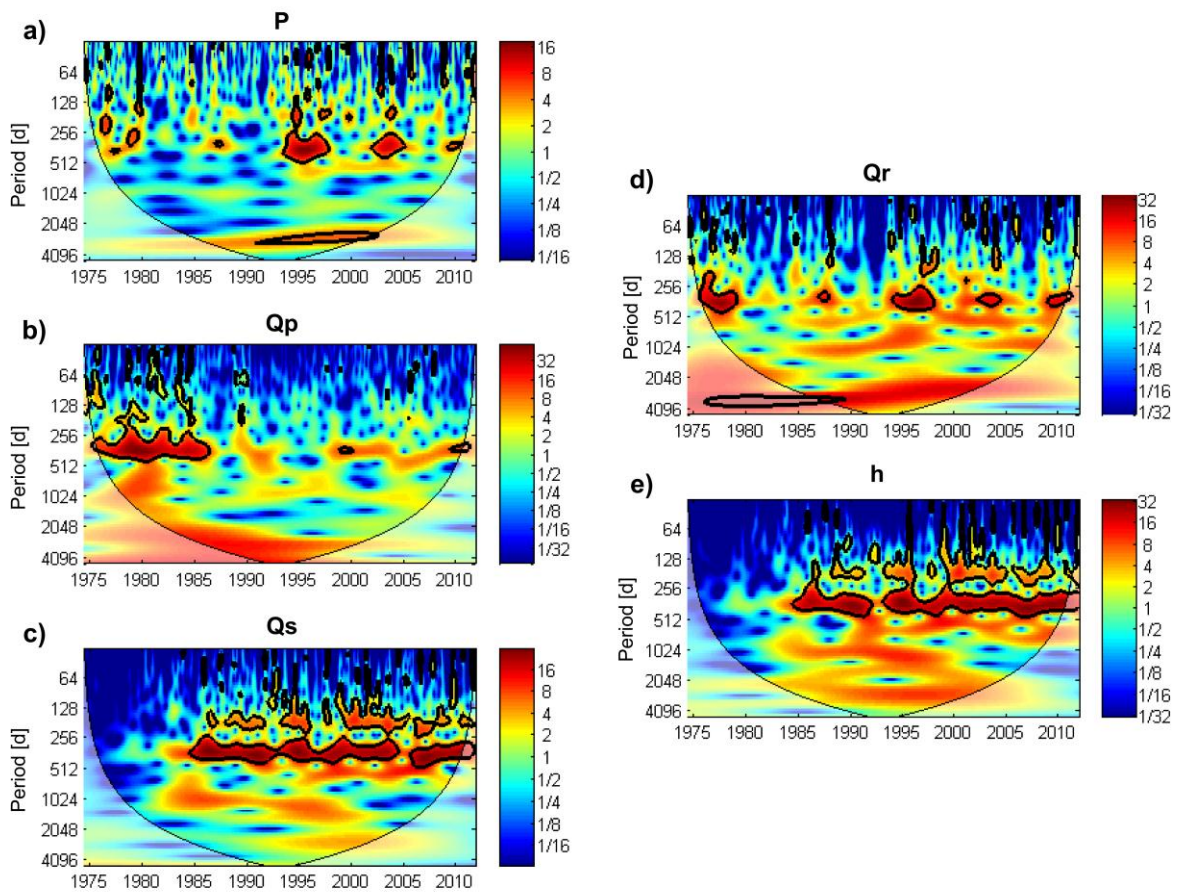
852 Figure 7: Cross-correlation functions (CCF) applied at different scales of the multiresolution  
 853 analysis with:  $P$ - $Q_r$  CCF (7a),  $Q_p$ - $s$  CCF (7b),  $Q_s$ - $Q_r$  CCF (7c), and  $Q_s$ - $s$  (7d); two cases are  
 854 shown for each plot: i) CCF between two signals at the same multiresolution level  $j$  (black  
 855 circles), and ii) CCF between an overall input signal (i.e. a non-decomposed time series) and  
 856 an isolated output signal at a given multiresolution level  $j$  (green stars). Maximum CCF  
 857 values ( $R_{max}$ ) are expressed as a function of the multiresolution levels in days (at level  $j$ , the  
 858 resolution corresponds to  $2^{j-1}$  days).  $R_{max}$  values are also plotted for CCF between two  
 859 overall signals (dashed blue line).



860

861

862 Figure 8: Continuous wavelet power spectra of the hydrogeological time series; the thick  
863 black outline designates the 5% significance level against red noise and the cone of influence,  
864 where edge effects might distort the picture, is shown in a lighter shade.

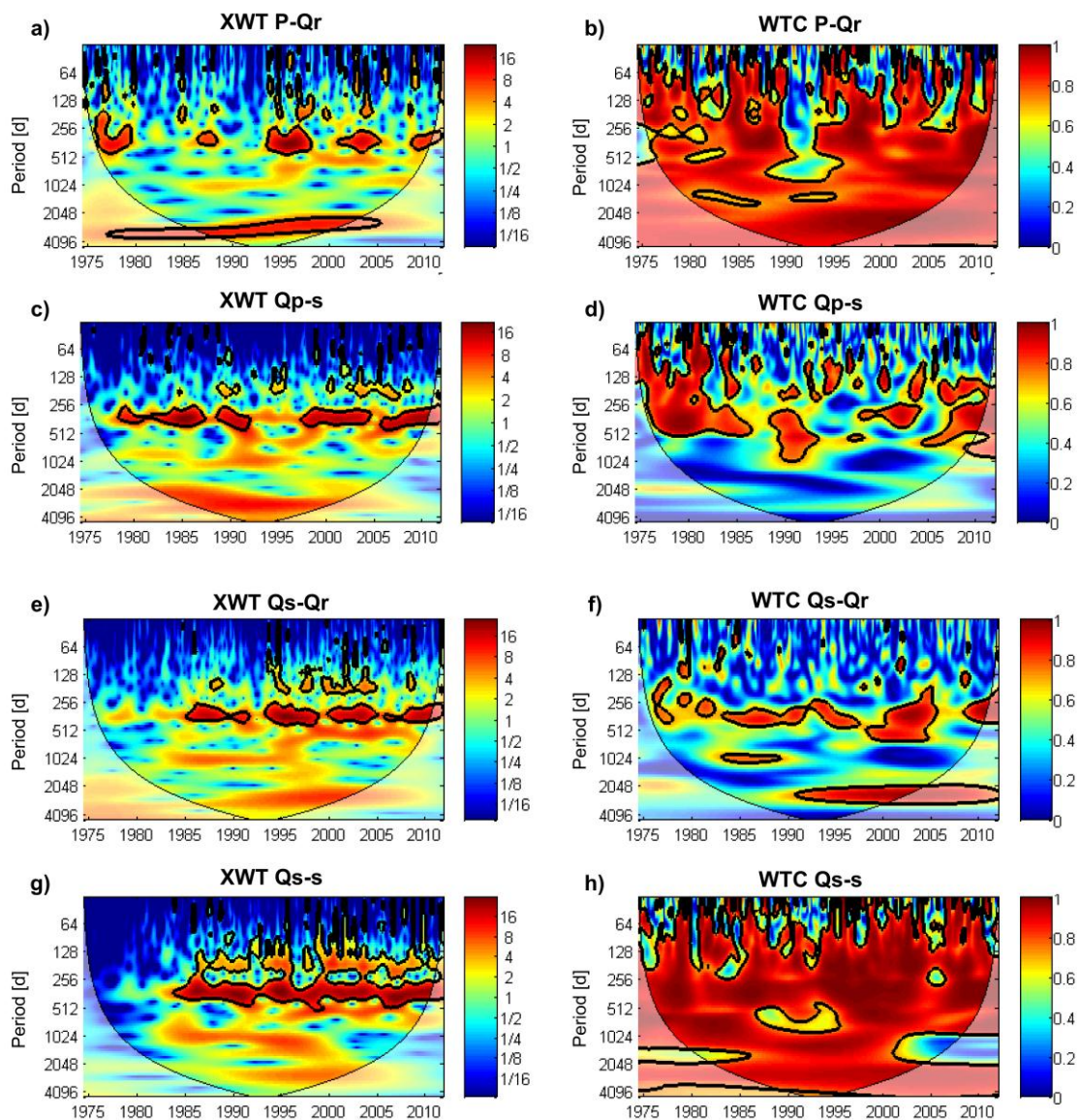


865

866



867 Figure 9: Cross wavelet (XWT) and wavelet coherence (WTC) spectra between (9a and 9b)  
 868 rainfall and residual Lez discharge  $P-Q_r$ , (9c and 9d) pumping and drawdown  $Q_p-s$ , (9e and  
 869 9f) groundwater stress and residual Lez discharge  $Q_s-Q_r$ , and (9g and 9h) groundwater stress  
 870 and drawdown  $Q_s-s$ ; The thick black outline designates the 5% significance level against red  
 871 noise and the cone of influence where edge effects might distort the picture is shown as a  
 872 lighter shade.



873